The Source of Saturn's G Ring
Matthew M. Hedman, *et al.*
Science **317**, 653 (2007);
DOI: 10.1126/science.1143964

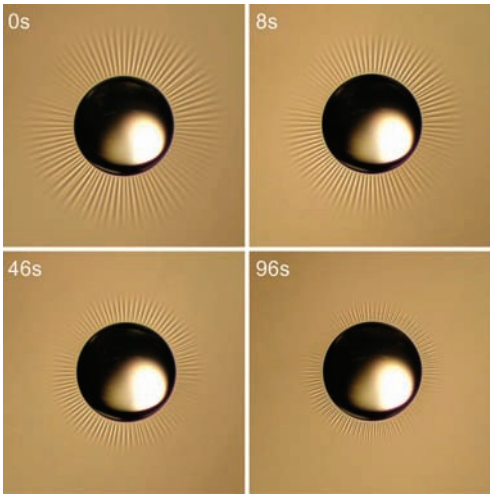

Fig. 5. (**A**) Relaxation of the wrinkle pattern as a function of time after loading with a water droplet. The thickness of the film h = 170 nm, and the mass fraction of the plasticizer is 35%. (**B**) The time dependence of wrinkle length L normalized by the length L_o, at the instant image capture commenced. Data are shown for plasticizer mass fractions of 35% (blue symbols) and 32% (red symbols). The plot symbols differentiate experimental runs, showing reproducibility of the time dependence. Solid lines show fits to a stretched exponential: $L(t)/L_o = \exp[-(t/\tau)^{\beta}]$.

(Fig. 4B) with our x-ray reflectivity measurements of h. Thus, measurements of both modulus and thickness can be achieved by a wrinkling assay with comparable or higher precision, and with very basic instrumentation, when compared to the other techniques on display in Fig. 4, each of which involves sophisticated equipment and yields only one of E or h.

Further, in contrast to the few other methods available for measuring the modulus of extremely thin films, such as nano-indentation (*13*) or stress-induced buckling (*12*), the measurement is performed with the film on a fluid surface, rather than mounted on a solid substrate. This allows the possibility for the film to relax internal mechanical stresses that can develop either in the spin-coating process or during transfer to a solid substrate. Apart from the ability to make measurements on a state that is not pre-stressed, this opens the possibility of measuring bulk relaxational properties of the film without concerns about pinning to a substrate. In Fig. 5A, we show a sequence of images visualizing the time-dependent relaxation of the wrinkle pattern formed by a capillary load. At increasing time, the wrinkles smoothly reduce in length and finally disappear. The strains that develop in response to the capillary load (*14*) can relax due to the viscoelastic response of the PS charged with a large mass fraction of plasticizer. In Fig. 5B, we show the time dependence of wrinkle length, $L(t)$, for two sets of films with different plasticizer mass fraction, x. $L(t)$ can be fit with a stretched exponential function $L_o \exp[-(t/\tau)^{\beta}]$, where τ decreases with increasing plasticizer concentration, and $\beta = 0.50 \pm 0.02$, typical of polymer viscoelastic response near the glass transition (*13*, *15*).

Thus, capillary-driven wrinkle formation can be used as the basis for a metrology of both the elastic modulus and the thickness of ultrathin films by means of a very elementary apparatus—a low-magnification microscope and a dish of fluid. This simple technique can also be used to study dynamical relaxation phenomena in ultrathin films.

References and Notes

1. E. Cerda, K. Ravi-Chander, L. Mahadevan, *Nature* **419**, 579 (2002).
2. E. Cerda, L. Mahadevan, *Phys. Rev. Lett.* **90**, 074302 (2003).
3. K. Efimenko *et al.*, *Nat. Mater.* **4**, 293 (2005).
4. J. Genzer, J. Groenewold, *Soft Matter* **2**, 310 (2006).
5. E. Cerda, *J. Biomech.* **38**, 1598 (2005).
6. T. P. Russell, *Mat Sci. Rep.* **5**, 171 (1990).
7. Supporting material is available on *Science* Online.
8. J.-C. Geminard, R. Bernal, F. Melo, *Eur. Phys. J. E* **15**, 117 (2004).
9. L. D. Landau, E. M. Lifshitz, *Theory of Elasticity, Course of Theoretical Physics* (Butterworth-Heinemann, India, ed. 3, 1986), vol. 7.
10. S. Timoshenko, J. Goodier, *Theory of Elasticity* (McGraw-Hill, New York, ed. 3, 1987).
11. J. Brandrup, E. H. Immergut, Polymer Handbook (Wiley, New York, ed. 3, 1989).
12. C. M. Stafford *et al.*, *Nat. Mater.* **3**, 545 (2004).
13. K. Miyake, N. Satomi, S. Sasaki, *Appl. Phys. Lett.* **89**, 031925 (2006).
14. H. Bodiguel, C. Fretigny, *Eur. Phys. J. E* **19**, 185 (2006).
15. N. G. McCrum, B. E. Reed, G. Williams, *Anelastic and Dielectric Effects in Polymeric Solids* (Wiley, London, 1967).

16. We acknowledge support from the Center for University of Massachusetts–Industry Cooperative Research Program (J.H.); the NSF–supported Materials Research Science and Engineering Center on Polymers at the University of Massachusetts (W.H.J.); the U.S. Department of Energy, Office of Basic Energy Science, through DE-FG-0296 ER45612 (T.P.R.); and the NSF through contracts NSF-DMR 0606216 (N.M.) and NSF-CBET-0609107 (T.S.E., T.P.R., and N.M.). We gratefully acknowledge useful conversations with A. D. Dinsmore.

Supporting Online Material

www.sciencemag.org/cgi/content/full/317/5838/650/DC1
Materials and Methods
Figs. S1 and S2

3 May 2007; accepted 15 June 2007
10.1126/science.1144616

The Source of Saturn's G Ring

Matthew M. Hedman,[1]* Joseph A. Burns,[1,2] Matthew S. Tiscareno,[1] Carolyn C. Porco,[3] Geraint H. Jones,[4,5] Elias Roussos,[4] Norbert Krupp,[4] Chris Paranicas,[6] Sascha Kempf[7]

The origin of Saturn's narrow G ring has been unclear. We show that it contains a bright arc located 167,495.6 ± 1.3 km from Saturn's center. This longitudinally localized material is trapped in a 7:6 corotation eccentricity resonance with the satellite Mimas. The cameras aboard the Cassini spacecraft mainly observe small (1 to 10 micrometers) dust grains in this region, but a sharp decrease in the flux of energetic electrons measured near this arc requires that it also contain larger (centimeter- to meter-sized) bodies whose total mass is equivalent to that of a ~100-meter-wide ice-rich moonlet. Collisions into these bodies may generate dust, which subsequently drifts outward to populate the rest of the G ring. Thus, the entire G ring could be derived from an arc of debris held in a resonance with Mimas.

The G ring is unique among Saturn's major rings in that, before the arrival of the Cassini spacecraft, there was no obvious explanation for its location. The dust-sized particles that dominate this ring's optical properties should erode quickly in Saturn's magnetosphere, yet there was no direct evidence for larger source bodies that could replenish the dust and no clear explanation for the concentration of such bodies in this one region (*1*–*5*). Unlike the E and F rings, which are closely associated with satellites that could either directly supply material to the ring (Enceladus) or potentially confine the ring particles into a narrow region (Prometheus and Pandora), the G ring is located 168,000 km from Saturn's center, over 15,000 km from the nearest known satellite. However, using data from the remote-sensing and in situ instruments onboard

[1]Department of Astronomy, Cornell University, Ithaca, NY 14853, USA. [2]Department of Theoretical and Applied Mechanics, Cornell University, Ithaca, NY 14853, USA. [3]Cassini Imaging Central Laboratory for Operations, Space Science Institute, Boulder, CO 94043, USA. [4]Max Planck Institut für Sonnensystemforschung, Katlenburg-Lindau 37191, Germany. [5]Mullard Space Science Laboratory, Department of Space and Climate Physics, University College London, Holmbury St. Mary, Dorking, Surrey RH5 6NT, UK. [6]Applied Physics Laboratory, Johns Hopkins University, Laurel, MD 20723, USA. [7]Max Planck Institut für Kernphysik, Saupfercheckweg 1, 69117 Heidelberg, Germany.

*To whom correspondence should be addressed. E-mail: mmhedman@astro.cornell.edu

the Cassini spacecraft, we have identified a structure that may be the source of this mysterious ring.

The Imaging Science Subsystem (ISS) onboard the Cassini spacecraft (*6*) obtained its most comprehensive view of the G ring on 19 September 2006, revealing a localized brightness enhancement near the ring's inner edge around 167,500 km from Saturn's center (Fig. 1). This feature extends over ~60° in longitude and has a radial full width at half maximum (FWHM) of ~250 km, much less than the ~6000-km radial extent of the entire G ring (see Figs. 2, 3).

At least five other image sequences obtained during the first 2 years of the Cassini mission observed this arc [Fig. 3 and supporting online material (SOM)], demonstrating that it is a persistent feature of the ring. Based on these measurements, we estimate that the arc's mean orbital motion is 445.475° ± 0.007°/day (period = 0.808126 ± 0.000013 day), where the uncertainty permits a 5° shift in the arc's position over 2 years. Given current measurements of Saturn's gravitational potential (*7*), this mean motion corresponds to an orbital semimajor axis a = 167,495.6 ± 1.3 km.

The arc's mean motion is extremely close to the Mimas 7:6 corotation eccentricity resonance (CER) at 445.484°/day (a = 167,493.4 km) (*8*). Corotation resonances have been invoked previously to explain arcs in Neptune's rings (*9*–*11*). In our case, perturbations from Mimas can constrain particles to librate around any of six stable longitudes λ where the resonant argument $\varphi_{CER} = 7\lambda_M - 6\lambda - \varpi_M$ equals 180° (λ_M and ϖ_M are the satellite Mimas' mean longitude and pericenter, respectively). An ensemble of such trapped particles could produce a longitudinally confined structure ~60° wide like the observed arc. Furthermore, throughout the first 2 years of the Cassini mission, the arc's peak has remained near one of the six stable points with $|\Delta\varphi_{CER}| < 40°$.

To verify this model, we conducted numerical simulations of 3830 massless test particles initially placed within 20 km of the Mimas 7:6 CER (see SOM). Most simulated particles (2820) were clearly trapped in the CER (with $|\Delta\varphi_{CER}| <$ 150°) over our 80-year integration. The dominant libration period was 1273 ± 3 days, significantly longer than the interval covered by the currently available observations. The marginally significant (0.009° ± 0.007°/day) drift in the arc's observed position relative to the stable points could therefore be part of a libration cycle. The mean epicyclic eccentricity of the simulated particles ranges from 0.0001 to 0.001 depending on $\Delta\varphi_{CER}$, consistent with the arc's ~250-km radial width (equivalent to an eccentricity ~ 0.0007).

Besides scattering light, the G ring and its arc also absorb magnetospheric particles, leaving detectable imprints on the local plasma environment. In fact, before Voyager took its first pictures of the G ring, Pioneer 11 detected subtle but persistent longitudinally averaged decreases (macrosignatures) in high-energy (<10 MeV) proton fluxes in this region (*12*). More recently, the Magnetospheric Imaging Instrument's Low Energy Magnetospheric Measurements System (LEMMS) onboard the Cassini spacecraft (which measures the flux of electrons with energies between 20 keV and 40 MeV) (*13*) has detected microsignatures (localized depletions in the electron flux) around the G ring. At ~12:13 universal time (UT) on 5 September 2005, this instrument observed an unprecedented ~50% decrease in electron flux while Cassini was moving outbound from Saturn (Fig. 2), and a candidate signature was detected inbound at ~11:58 UT. Two previous passages near the G ring did not show a strong absorption (see SOM).

Using the arc's orbital period determined above, Cassini's location relative to the arc can be plotted for all three passages near the G ring (Fig. 4). The 5 September 2005 passage was much closer to the arc than the others and, when mapped to the equatorial plane, the outbound microsignature's radial profile was 250 km wide, consistent with the arc's inferred density profile (Fig. 2). The absorption signature is most apparent in the LEMMS channels that measure mega–electron volt electrons. Electrons with energies around 1 MeV near the G ring have net azimuthal speeds close to the Keplerian orbital rate, allowing for the formation of very deep absorption signatures. These data strongly suggest that material associated with the arc caused the deep absorption.

The inferred position of the outbound microsignature in Saturn's equatorial plane is displaced roughly 3000 km exterior to the arc (Fig. 2), but this is not too surprising because similar displacements are observed in the signatures of Saturn's small and mid-sized satellites (*14*, *15*). Depletions in charged particles will drift and fill in at different rates, depending on the electrons' energies and the pitch angles of the electrons' trajectories around the magnetic field lines, so the

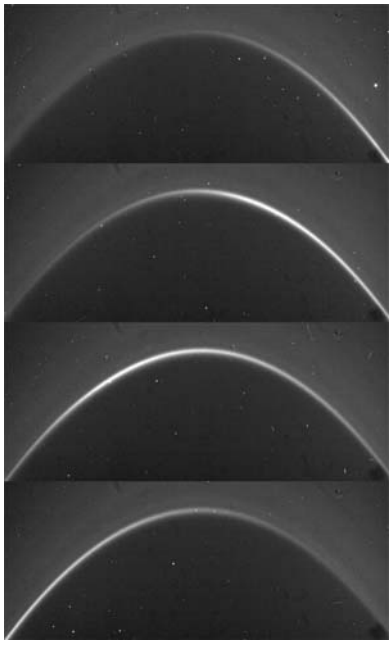

Fig. 1. Images of the G ring arc obtained on 19 September 2006 at 12:37, 13:11, 13:44, and 14:18 UTC from top to bottom. A bright arc moves from right to left through the field of view.

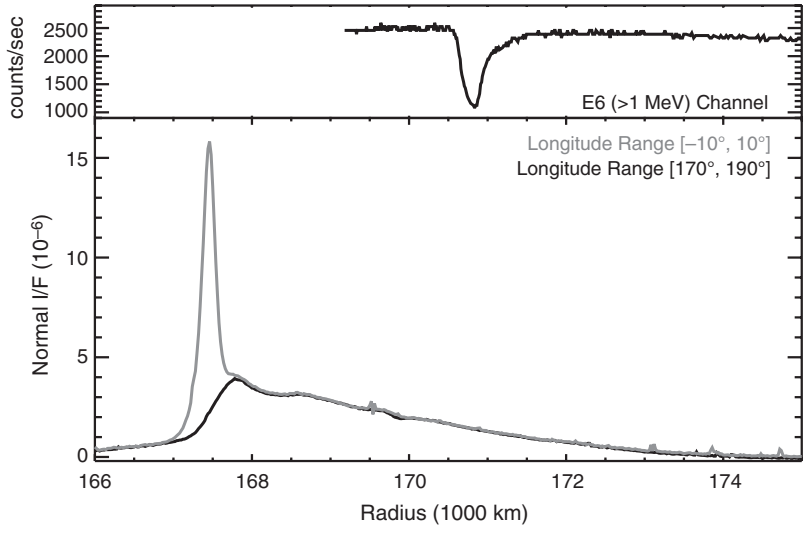

Fig. 2. (**Top**) The charged-particle flux detected by LEMMS channel E6 (*13*, *15*) during Cassini's passage over the arc region on 5 September 2005. The radial scale here corresponds to the equatorial distance of the unperturbed magnetic field lines that thread Cassini at the time of the observation. (**Bottom**) Average (offset-subtracted) radial brightness profiles of the G ring at different longitudes relative to the arc's peak based on data from 19 September 2006. The profiles through the arc (gray) and elsewhere (black) are essentially identical outside 168,000 km, whereas the arc is the sharp peak at 167,500 km in the gray profile. The absorption feature's radial width is comparable to the visible arc's. The 3000-km radial offset between the two signatures may be caused by magnetospheric effects (see SOM).

microsignature could be displaced by larger-scale magnetospheric processes or through a deformation of the local magnetic field by the arc itself.

For a given set of electron pitch angles (near 30° during this observation) and energies (which determine the electron's drift rate relative to the arc), and assuming absorbers composed primarily of water ice, the total arc mass can be estimated from the magnitude of the LEMMS absorption (*16*). For energies between 1 and 10 MeV, the observed depletion implies a total mass between 10^8 and 10^{10} kg (see SOM). If all this material were gathered into a single body, that object would be roughly 100 m across. Because the gyroradii of 1-MeV electrons are on the order of a few kilometers here, the absorption signature's 250-km width indicates that this mass is not in a single body but is instead distributed among multiple objects.

The arc observed in imaging data has a peak normalized reflectance (or normal *I*/*F*, see SOM) that increases from 10^{-6} to 10^{-5} between phase angles of 90° and 165°. Such strong forward scattering implies that the cameras mostly see dust grains 1 to 10 μm across (*17*). The *I*/*F* values indicate that the normal optical depth in this dust is ~10^{-5}, implying that the entire arc contains between 10^5 and 10^6 kg of dust, which is much less than the absorbing mass required by the in situ data. The arc must therefore contain a population of larger particles ranging from centimeters to meters across. The size distribution of these larger objects is not strongly constrained, but if we assume for simplicity that the larger bodies in the arc are on average ~1 m across, their total optical depth would only be around 10^{-7}, well below our current optical detection limit and comparable to previous estimates based on Voyager and Pioneer data (*1*). We propose that impact ejecta from these objects supply the dust that forms not only the visible arc but ultimately also the rest of the G ring.

The bulk of the visible G ring lies exterior to the arc, and the radial brightness profile of the outer part of the G ring decays exponentially with a scale length of approximately 3500 km (*18*) (Fig. 2). Curiously, the Cosmic Dust Analyzer's (CDA) High Rate Detector (HRD) onboard the Cassini spacecraft (*19*) recorded an impact with an exceptionally large dust grain at 10:38:25 UT on 5 September 2005, when the spacecraft passed through the ring plane at 176,700 km, near the outermost edge of the visible G ring. Although the exact size of this grain is uncertain, it produced damage that was never observed in laboratory experiments with grains less than 100 μm across, so this grain was probably at least 100 μm in size. We can explain both of these phenomena with a simple model similar to one

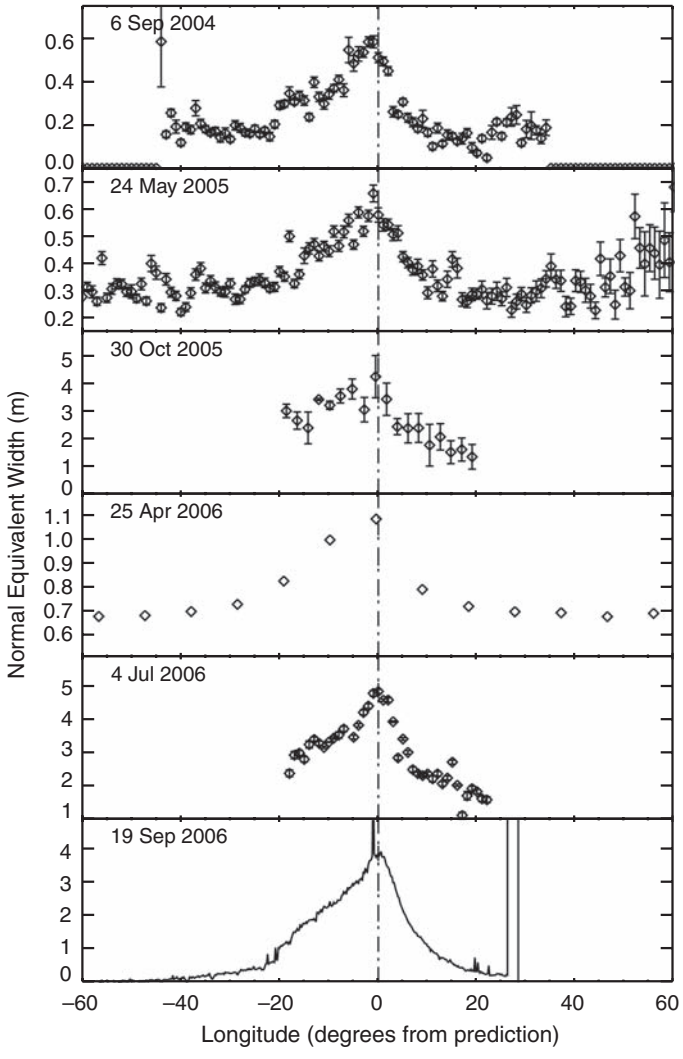

Fig. 3. Six profiles of the G-ring arc's radially integrated brightness (see SOM) versus longitude relative to a coordinate system rotating with a mean motion of 445.475°/day. Errors are based on random noise in the images. These errors are 0.02 and 0.1 m for the 25 April 2006 and 19 September 2006 data, respectively, and so are not plotted. The arc's longitudinal extent is <60°, as expected for a collection of particles trapped in a 7:6 resonance.

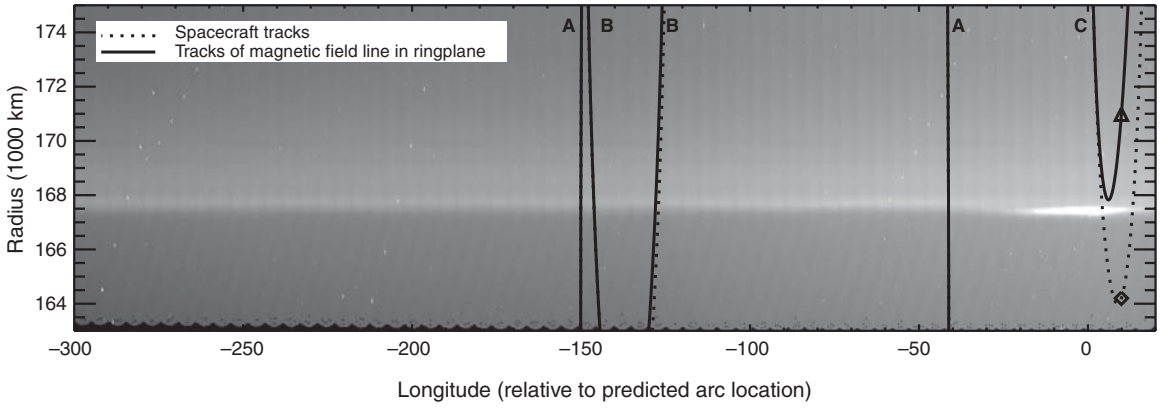

Fig. 4. Correlation between remote-sensing and in situ data. The background image shows the G ring's brightness as a function of radius and longitude measured relative to the arc's center (at 0°). The dotted lines trace Cassini's orbit during its three passages through this region (A = 1 July 2004, B = 14 April 2005, C = 5 September 2005). The solid lines show where an unperturbed magnetic field line threading through the spacecraft would intersect the ring plane during these times. The triangle and diamond mark the time of the strongest absorption detected by LEMMS on 5 September 2005 (Fig. 2).

previously proposed for other dusty rings (*17*, *20*), where small grains released from the arc drift outward under the influence of nongravitational drag forces (such as plasma drag) while they are steadily eroded by collisions with ions, atoms, and smaller grains.

Consider that the visible arc represents dust released from the surfaces of larger bodies by collisions. Although the source bodies are trapped in the Mimas resonance, interactions with Saturn's magnetosphere allow dust to escape this region (*17*). The magnetospheric plasma corotates with the planet's magnetic field (period ~ 0.45 days) (*21*), so its mean motion is much faster than the dust grains' Keplerian orbital motion. Momentum transfer from the plasma therefore causes the dust to drift outward over time. For a particle of mass m located at semimajor axis a and with an orbital velocity v, a drag force F_D will cause a motion $da/dt = a/v(F_D/m)$. In general, F_D is proportional to the particle's surface area whereas m is proportional to its volume, so $da/dt \propto 1/s$, where s is the dust grain's linear size.

As the dust grains drift outward, they will be steadily eroded by collisions with plasma ions, energetic particles, and other small grains. So long as the collisions do not completely shatter the drifting grain (*17*), the mass loss rate will be proportional to the impactor flux times the grain's cross-sectional area, so $dm/dt \propto s^2$ and $ds/dt \propto s^0$. Thus, $ds/da \propto s$. Given that the G ring is narrow ($\delta a/a \sim 0.05$) and assuming that the drag forces and erosion rates do not vary significantly across this region, s should therefore decay exponentially with distance from the source region δa; that is, $s = s_o e^{-\delta a/3D}$, where s_o is the initial particle size, e is the base of natural logarithms, and $3D$ is a scale length determined by the orbital and magnetospheric environments.

The G ring's brightness and optical depth τ at a given δa are proportional to the integral of the particle cross section over the differential particle size distribution at that location [$\tau = \int \pi s^2 n(s,\delta a) ds$]. Assuming that the ring is in a steady state, continuity requires that the number flux of particles of a size s at a distance δa from the arc equal the flux of particles of size s_o released from the arc, which requires that $n(s,\delta a) = n(s_o,0)$ (see SOM). Hence, τ scales like s^3 and the optical depth also decreases exponentially with radial distance from the arc/source, but with a scale length of D instead of $3D$: $\tau = \tau_o e^{-\delta a/D}$. This simple, generic model therefore produces a radial brightness profile with the same basic shape as that observed in the remote-sensing data. Furthermore, the shorter scale length in the optical depth means that although the brightness of the ring at 176,700 km is reduced by over an order of magnitude, individual particle sizes are reduced by only a factor of 2 or 3, so the grain detected by CDA could have been as small as about 200 μm across when it escaped the arc (that is, still small enough to be subject to nongravitational accelerations).

References and Notes

1. M. R. Showalter, J. N. Cuzzi, *Icarus* **103**, 124 (1993).
2. R. Canup, L. W. Esposito, *Icarus* **126**, 28 (1997).
3. H. B. Throop, L. W. Esposito, *Icarus* **131**, 152 (1998).
4. J. J. Lissauer, R. G. French, *Icarus* **146**, 12 (2000).
5. I. dePater, S. C. Martin, M. R. Showalter, *Icarus* **172**, 446 (2004).
6. C. C. Porco *et al.*, *Space Sci. Rev.* **115**, 363 (2004).
7. R. A. Jacobson *et al.*, *Astron. J.* **132**, 2520 (2006).
8. Mimas' 7:6 inner Lindblad resonance also lies nearby at 445.411°/day (a = 167,511 km).
9. P. Goldreich, S. Tremaine, N. Borderies, *Astron. J.* **92**, 490 (1986).
10. C. C. Porco, *Science* **253**, 995 (1991).
11. F. Namouni, C. C. Porco, *Nature* **417**, 45 (2002).
12. J. A. van Allen, *J. Geophys. Res.* **88**, 6911 (1983).
13. S. M. Krimigis *et al.*, *Space Sci. Rev.* **114**, 233 (2004).
14. G. H. Jones *et al.*, *Science* **311**, 1412 (2006).
15. E. Roussos *et al.*, *Icarus*, in press.
16. J. N. Cuzzi, J. A. Burns, *Icarus* **74**, 284 (1988).
17. J. A. Burns, D. P. Hamilton, M. R. Showalter, in *Interplanetary Dust*, E. Grün, B. Gustafson, S. Dermott, H. Fechtig, Eds. (Springer, New York, 2001), pp. 641–725.
18. Slight deviations from an exponential profile occur around 168,200 and 169,800 km. The latter feature shows longitudinal structure and is probably associated with the Mimas 8:7 inner Lindblad resonance.
19. R. Srama *et al.*, *Space Sci. Rev.* **114**, 465 (2004).
20. J. A. Burns, M. R. Showalter, G. E. Morfill, in *Planetary Rings*, R. Greenberg, A. Brahic, Eds. (Univ. of Arizona Press, Tucson, AZ, 1984), pp. 200–272.
21. D. Gurnett *et al.*, *Science* **316**, 442 (2007).

22. We thank the staff at the Space Science Institute, Jet Propulsion Laboratory, and Cornell University for planning and delivering the imaging data, and M. Kusterer of the Johns Hopkins University Applied Physics Laboratory (JHUAPL) for LEMMS data reduction. We also acknowledge the support of the Cassini Project and NASA's Planetary Geology & Geophysics program. MIMI/LEMMS was in part financed by the German Bundesministerium für Bildung und Forschung through the German Aerospace Center (DLR) under contract 50 OH 0103 and by the Max Planck Gesellschaft. The work at JHUAPL was supported by NASA under contract NAS5-97271 with the Johns Hopkins University. G.H.J. was partially supported by the Science and Technology Facilities Council, UK.

18 April 2007; accepted 14 June 2007
10.1126/science.1143964

The FERONIA Receptor-like Kinase Mediates Male-Female Interactions During Pollen Tube Reception

Juan-Miguel Escobar-Restrepo,[1] Norbert Huck,[1] Sharon Kessler,[1] Valeria Gagliardini,[1] Jacqueline Gheyselinck,[1] Wei-Cai Yang,[2] Ueli Grossniklaus[1]*

In flowering plants, signaling between the male pollen tube and the synergid cells of the female gametophyte is required for fertilization. In the *Arabidopsis thaliana* mutant *feronia* (*fer*), fertilization is impaired; the pollen tube fails to arrest and thus continues to grow inside the female gametophyte. *FER* encodes a synergid-expressed, plasma membrane–localized receptor-like kinase. We found that the FER protein accumulates asymmetrically in the synergid membrane at the filiform apparatus. Interspecific crosses using pollen from *Arabidopsis lyrata* and *Cardamine flexuosa* on *A. thaliana* stigmas resulted in a *fer*-like phenotype that correlates with sequence divergence in the extracellular domain of FER. Our findings show that the female control of pollen tube reception is based on a *FER*-dependent signaling pathway, which may play a role in reproductive isolation barriers.

In contrast to animals, where the products of meiosis differentiate directly into gametes, the meiotic products of higher plants undergo further mitotic divisions to form multicellular haploid structures called gametophytes, which in turn produce the gametes. To accomplish fertilization, the gametophytes communicate with and recognize each other. In angiosperms, the male gametophyte (pollen) germinates on the stigma and the growing pollen tube delivers the two nonmotile sperm cells to the female gametophyte (embryo sac). Proper delivery depends on signals from the female gametophyte (*1*, *2*). These chemotactic signals guide the pollen tube into the micropylar opening of the ovule, the reproductive structure that harbors the female gametophyte. In the majority of flowering plants, including *Arabidopsis thaliana* (Brassicaceae), the female gametophyte consists of seven cells: the egg cell, the two synergids (which lie just inside the micropylar opening of the ovule), the central cell, and the three antipodals (*3*) (Fig. 1A). In *Torenia fournieri* (Scrophulariaceae), the two synergids are necessary for pollen tube guidance (*4*). In most species, one of the synergids degenerates prior to or coincident with the pollen tube approaching the micropyle (*5*). The pollen tube grows into the degenerating synergid through the filiform apparatus, a structure formed by invaginations of the cell wall of

[1]Institute of Plant Biology and Zürich-Basel Plant Science Center, University of Zürich, Zollikerstrasse 107, CH-8008 Zürich, Switzerland. [2]Key Laboratory of Molecular and Developmental Biology, Institute of Genetics and Developmental Biology, Chinese Academy of Sciences, Beijing 100101, China.

*To whom correspondence should be addressed. E-mail: grossnik@botinst.uzh.ch

Supporting Online Material for

The Source of Saturn's G Ring

Matthew M. Hedman,* Joseph A. Burns, Matthew S. Tiscareno, Carolyn C. Porco, Geraint H. Jones, Elias Roussos, Norbert Krupp, Chris Paranicas, Sascha Kempf

*To whom correspondence should be addressed. E-mail: mmhedman@astro.cornell.edu

Published 3 August 2007, *Science* **317**, 5838 (2007)
DOI: 10.1126/science.1143964

This PDF file includes:

Supporting Online Material for "The Source of Saturn's G Ring":

Supporting Text:

Image Processing

Casssini images of the G ring were calibrated using the standard pipeline (*S1*), which converts raw data numbers into measurements of *I/F*, the ratio of brightness of the scene to that of a perfect Lambert surface at normal incidence. To account for differences in the viewing geometry, these brightness estimates were then multiplied by μ (the sine of the ring opening angle) to obtain the brightness of the ring viewed at normal incidence, known as the "normal *I/F*".

The appropriate spacecraft and trajectory SPICE kernels were used to geometrically navigate the images. The positions of known stars in the field of view were then used to refine the pointing, and to obtain the equatorial radius and longitude of each pixel in the image. With this information, we azimuthally averaged the signal to produce radial profiles like those shown in Fig. 1, or re-projected the data onto grids in radius and longitude to make maps like that shown in Fig. 4.

The longitudinal profiles shown in Fig. 3 derive from six sequences of images (See Table S1). During each sequence the camera watched material rotate through a certain inertial longitude in the G ring. For most of these sequences, the images were first re-projected onto a grid of radii and (inertial) longitudes, then for each longitude bin we integrated the normalized brightness over orbital radius to obtain the normal equivalent width $\int \mu I/F \, dr$. This quantity is used instead of the peak *I/F* value because equivalent width is relatively insensitive to image resolution (*S2*). The integration range is chosen separately for each sequence in order to capture the entire arc signal. A combined profile for each sequence was constructed from the individual image profiles assuming the arc orbits Saturn at a fiducial rate (445.475 ^{0}/day). This final profile consists of the average equivalent width measured within each corotating longitude bin, and the error bars are computed based on the variance of the equivalent-width estimates within each bin. Note that in the 19 Sep 2006 data we also subtract a background level.

The data sets from 30 Oct 2005 and 25 Apr 2006 were processed slightly differently from the others because these sequences were taken at very small ring-opening angles ($<0.5^0$), which meant that the data could not be re-projected onto a radius/longitude grid without significant distortion. For these data sets we obtained a single radial profile of the G ring from each image, and computed an effective longitude for that scan based on the spacecraft position. The equivalent width was then computed for each profile. For the 30 Oct 2005 observations the resulting data are binned in longitude to improve signal-to-noise.

Numerical Simulations

We conducted numerical simulations of 3,830 massless test particles near the Mimas 7:6 CER. Particle orbits about Saturn were evolved under the influence of Mimas as well as eight other saturnian moons, the Sun, and Jupiter. Saturn's J_2 and J_4 harmonic coefficients (*S3*), resulting from the planet's oblateness, were also accounted for. Inter-particle collisions were neglected, due to the G Ring's low optical depth. The integrations were carried out using software based on the Swift package (*S4-S6*). The orbits of the massive perturbers were not directly integrated; rather, their positions at each time step were obtained from JPL ephemeris kernels DE414 and SAT252 (*S7*). The test particles were directly integrated for 80 years – 1 Jan 1970 to 1 Jan 2050, the entire length of time available in the ephemerides for the massive perturbers.

Because standard (osculating) orbital elements can behave pathologically under an oblate central mass, varying significantly on orbital timescales, we use epicyclic orbital elements (*S8-S11*) to define input parameters and to analyze the simulation outputs, as well as in all discussions below. The simulation code itself uses Cartesian coordinates for input and output.

All particles began with their epicyclic eccentricity and inclination set to zero. Initial epicyclic semi-major axis ranged from 167,472.5 to 167,510.5 km, sampling the phase space surrounding the Mimas 7:6 corotation eccentricity resonance (CER, resonant argument $\varphi_{CER} = 7\lambda_{Mimas} - 6\lambda_{arc} - \varpi_{Mimas}$), while longitudes covered 0^o to 66^o, sampling the full phase space around one of the six CER co-rotation sites.

Most simulated particles (2,820) are clearly trapped in the CER, with $|\Delta\varphi_{CER}| < 150^o$. Confinement in the resonance is effective, with no significant leakage over the 80-year integration.

The dominant period for libration of the semimajor axis is 1273 +/- 3 days (Figure S1b), though the period increases for very loosely bound particles ($|\Delta\varphi_{CER}| > 130^o$). Also present in the semimajor-axis libration is a long period resulting from Mimas' own motion under its 4:2 resonance with Tethys. This libration, which is slow enough that test particles move adiabatically along with Mimas, has a period of ~72 yr (*S12,S13*) and imparts to resonant test particles an amplitude of ~4 km in semimajor axis. Other weaker frequencies are also present in both librations.

The libration of the resonant argument also has a dominant period of 1273 +/- 3 days for $|\Delta\varphi_{CER}| < 130^o$. Secondary frequencies are generally different from the secondary frequencies in the semimajor axis, with 596 +/- 3 days being the second-most prominent period.

The width of the resonance is given by the amplitude of the semimajor axis libration, which increases directly with the resonant argument libration amplitude and which is a measure of how tightly bound to the resonance a test particle is. The most loosely bound

particles that are still in the resonant phase space have $\Delta a \sim 35$ km (Figure S1a); subtracting the 4 km due to Mimas' 72-year libration gives a resonance width of 31 km.

Since all test particles began in circular coplanar orbits, the eccentricity and inclination forced by outside perturbations can be estimated from the mean values of the epicyclic eccentricity and inclination over the integration's lifetime. More tightly bound particles tend to have lower e and i, with characteristic values being $e \sim 0.001$ (Figure S1c) and $i \sim 0.003^{o}$ (Figure S1d).

The dominant simulated libration period of 1273 days is significantly longer than the interval covered by the currently available observations (743 days). Thus far we have seen the arc run slightly slower than the resonance, beginning slightly ahead of a corotation site and drifting behind it. This can be explained as simply part of a libration cycle; if this is correct, we would expect to discern a turnaround in the next year or two, with the arc speeding up and overtaking the corotation site again.

We can explain the observed radial width of the arc (~250 km) with a combination of the resonance width and the forced eccentricities in our simulations. The resonance width (i.e., the range of semimajor axes among resonant particles) is 31 km; subtracting this from the observed value, we are left to account for ~220 km of radial width. This corresponds to an eccentricity $e \sim 0.0007$ (given the semimajor axis $a \sim 167{,}500$ km), which is consistent with the simulated forced eccentricities (Figure S1c).

LEMMS observations during G-ring crossings

Cassini crossed regions magnetically connected to the G-ring during three orbits, for six total passes inbound and outbound. Figures S2-S5 show despiked time series of count rates in the LEMMS channels E4-E6 with the electron pitch angles observed by the spacecraft (*S14*,*S15*).

Fig. S2 and S3 show the data from 1 July 2004. The sinusoidal variations in the count rates occur because LEMMS scanned continuously through a range of pitch angles during these observations. These oscillations complicate interpretation of these data, but there is no evidence for a strong absorption in these data. Subtle variations in the electron flux may be present in the data, but they would be considerably weaker than the strong absorption seen in Fig.3.

Fig. S4 shows the data from 14 Apr 2005. There are no absorption signatures visible in either the inbound or outbound data.

Fig. S5 shows the full time series of the 5 Sep 2005 pass. The strong absorption can be seen clearly at ~12:13 UTC. Other shifts in the level are associated with changes in spacecraft orientation. However, the small dip at ~11:58 may represent a second absorption signature. Unfortunately, this occurs during a spacecraft turn, so it is difficult to say whether this feature is really a second microsignature associated with the G ring or its arc.

Despite the evidence for possible variations absorptions on previous crossings, these features are not nearly as strong as that observed at ~12:13 on 5 Sep 2005. Furthermore, Pioneer 11 and Voyager 2 also crossed the G-ring a total of four times and did not record anything peculiar in their energetic electron detectors. The presence of the G-ring therefore cannot explain the sharp electron absorption seen on 5 Sep 2005. Given the proximity of Cassini to the G-ring arc at this time, the additional material contained in this structure is most likely responsible for the electron absorption.

Arc inclination and the absorption signature displacement

Given the elevation of the spacecraft above the ring plane (Fig. S6) and the radial displacements of microsignatures of small and mid-sized satellites (*S15*,*16*), we interpret the ~3000 km displacement of the 5 Sep 2005 absorption signature relative to the visible arc's location as the result of magnetospheric phenomena. One possible alternative explanation is that the arc moves on an inclined orbit. An inclined orbit could bring the arc to higher (magnetic) latitudes, which in turn means that the arc would thread different field lines that have their equatorial location (L-shell) at larger distance. Therefore the inclination can lead to outward displacements of the arc's electromagnetic imprint, as observed.

Assuming that the arc's inclination is i, then the maximum latitude that the arc can reach is also i. The shape of a field line as a function of latitude in a dipole field is given by $r = L\cos^2\varphi$, where r is the radial distance, L is the equatorial field line distance (L-shell) and φ is the latitude. Using $\varphi=i$, and from observations, r=167500 km, and L=170789 km, we get that $i\sim 8^0$. Corrections for the fact that the magnetic equator is northwards displaced compared to the kronographic equatorial plane, can lower this not less than 4^0.

Nearly edge-on observations of the G Ring (Images N1524626870-N1524639589, ring-opening angle ~0.07^0) place an upper limit of ~100 km on the vertical thickness, corresponding to a maximum allowable inclination of 0.02^o. This is consistent with the simulated forced inclinations, which are far smaller (Figure S1d). Furthermore, if the entire G ring does derive from the arc, a finite inclination in the arc would produce a finite vertical thickness in the entire ring. Edge-on views of the ring show the visible G ring is less than 200 km thick. The arc's inclination is therefore unlikely to be large enough to explain the arc's displacement.

LEMMS Estimates of the Arc's Mass

This analysis uses procedures described in (*S15*). The electron flux (measured in counts per second or *CPS*) during the outbound 5 Sep 2005 microsignature reached a minimum value CPS_{final} of ~50% the background level outside the microsignature ($CPS_{initial}$) . We can therefore define the following measure of the strength of the absorption:

$$f = -0.5\ln\left(\frac{CPS_{final}}{CPS_{initial}}\right) \sim 0.2 \qquad (1)$$

such that the total column mass of material along the electrons' paths is $K=fR$, where the "range" R is the column mass of material required to attenuate the population of penetrating electrons by a factor of e^2. This range depends only on the electrons' energy and the material. Assuming water ice and 1 MeV electrons, $R \sim 1$ g/cm^2 (*S17*).

The column mass K is related to the arc's total mass M by the following approximate expression (derived from equation (7) in *S18*):

$$M = 0.5\, w\, KVT_b \cos\theta_{eq}, \quad (1)$$

where $\theta_{eq} \sim 35^0$ is the equatorial pitch angle, $w \sim 250$ km is the radial width of the arc, T_b is the electron bounce period and V is the bounce-averaged velocity of the electrons relative to the arc, which depend the particle's energy E and θ_{eq} *(S19)*.

Using the above values we get that:

$$M \sim (2*10^6 \text{ cm})\, RVT_b \quad (3)$$

The remaining terms depend on the electron energy E, so Figure S7 shows M as a function of E. Near 1 MeV M falls to approximately 10^8 kg because at this energy the drift velocity V is close to the keplerian orbital velocity, so electrons can spend a long time passing through the arc, and lower masses are needed to produce a given absorption. At other energies the total mass must be around 10^{10} kg.

Calculation of optical depth profile of the outer G ring:

The optical depth τ of the ring at a given δa away from the arc is given by the integral:

$$\tau = \int \pi s^2\, n(s,\delta a)\, ds, \quad (4)$$

where s is the particle size and $n(s,\delta a)$ is the differential particle size distribution at a distance δa away from the source region. Assuming the ring is in a steady state, there must be as many particles drifting into a given orbit as drifting out of it. Hence the number flux of particles of size s across a given δa must be the same as the number flux of particles of size s_0 at δa=0. In other words, $v_a(s,\delta a)\, n(s,\delta a)\, ds = v_a(s_0,0)\, n(s_0,0)\, ds_0$, where v_a is the radial velocity of the particles. Assuming the particle size decays exponentially with distance from the arc like $s=s_o e^{-\delta a/3D}$, then $ds = e^{-\delta a/3D}\, ds_o$. Furthermore, since $v_a = da/dt \propto 1/s$, $v_a(s,\delta a) = v_a(s_0,0) e^{+\delta a/3D}$. The conservation of flux thus requires that $n(s,\delta a) = n(s_0,0)$.

Therefore, $\tau = \int \pi s^2\, n(s,\delta a)\, ds = \int \pi s_0^2\, n(s_0,0)\, ds = e^{-\delta a/D} \int \pi s_0^2\, n(s_0,0)\, ds_0 = \tau_o e^{-\delta a/D}$.

Supporting Figures:

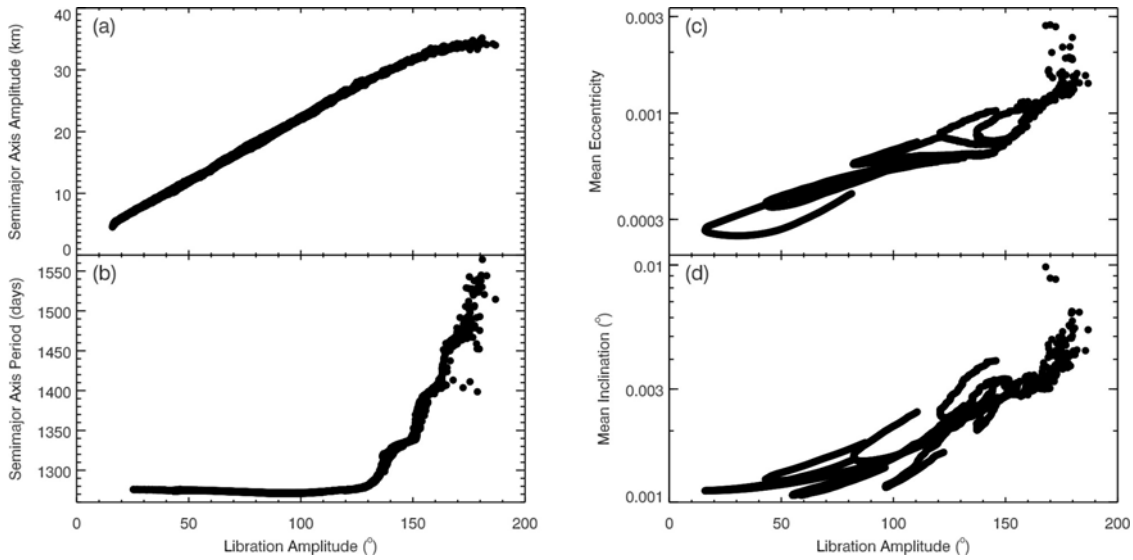

Figure S1: Attributes of simulated resonant particles, plotted against amplitude of resonant argument libration. (a) amplitude of semimajor axis libration, (b) dominant period of semimajor axis libration, (c) mean eccentricity over the 80-year integration, (d) mean inclination over the 80-year integration.

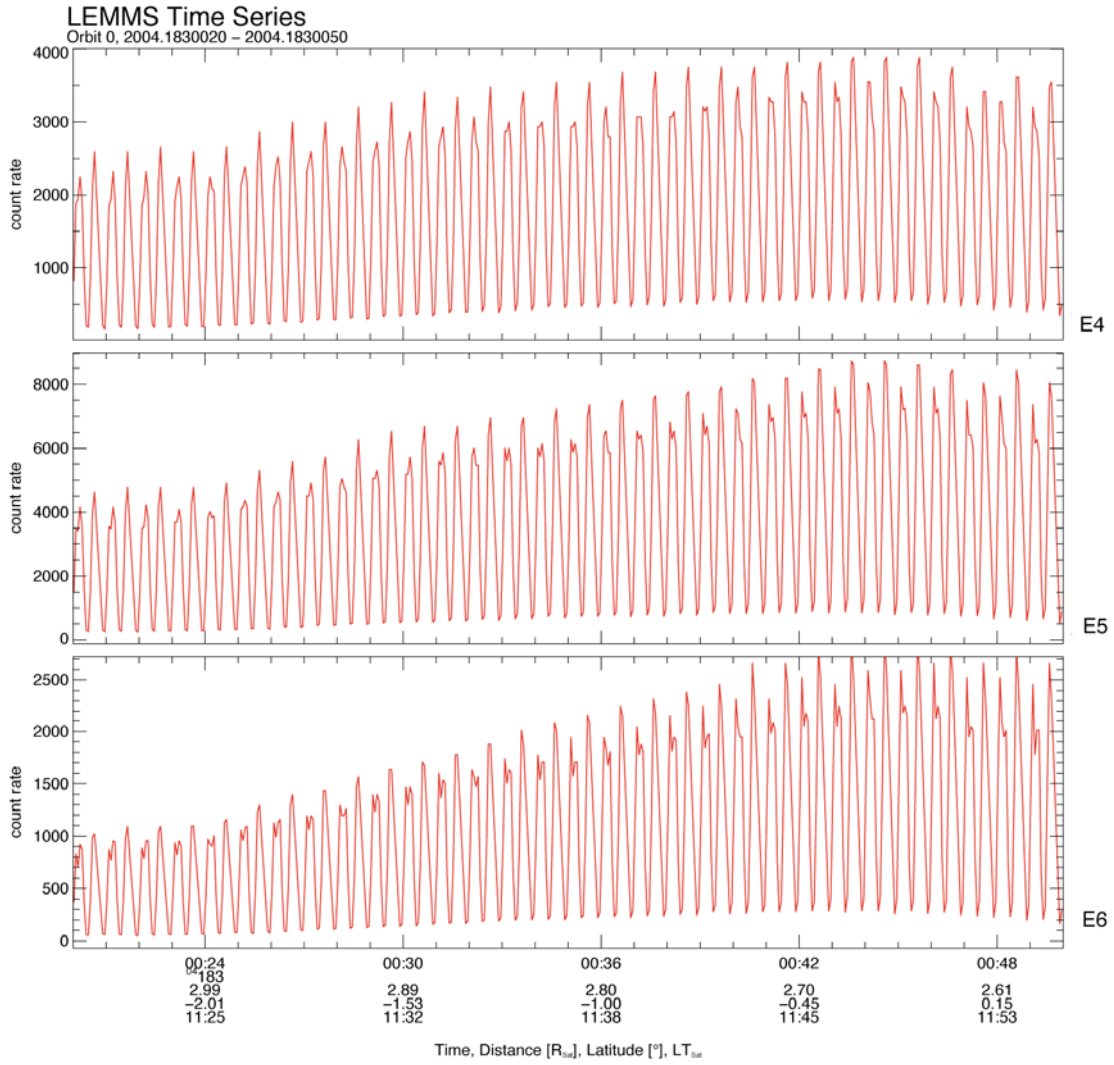

Figure S2: LEMMS data taken during the inbound G-ring crossing of 1 July 2004. Each panel shows the time series in one LEMMS channel. Sinusoidal variations in the fluxes occur because the instrument continuously scanned over a range of pitch angles.

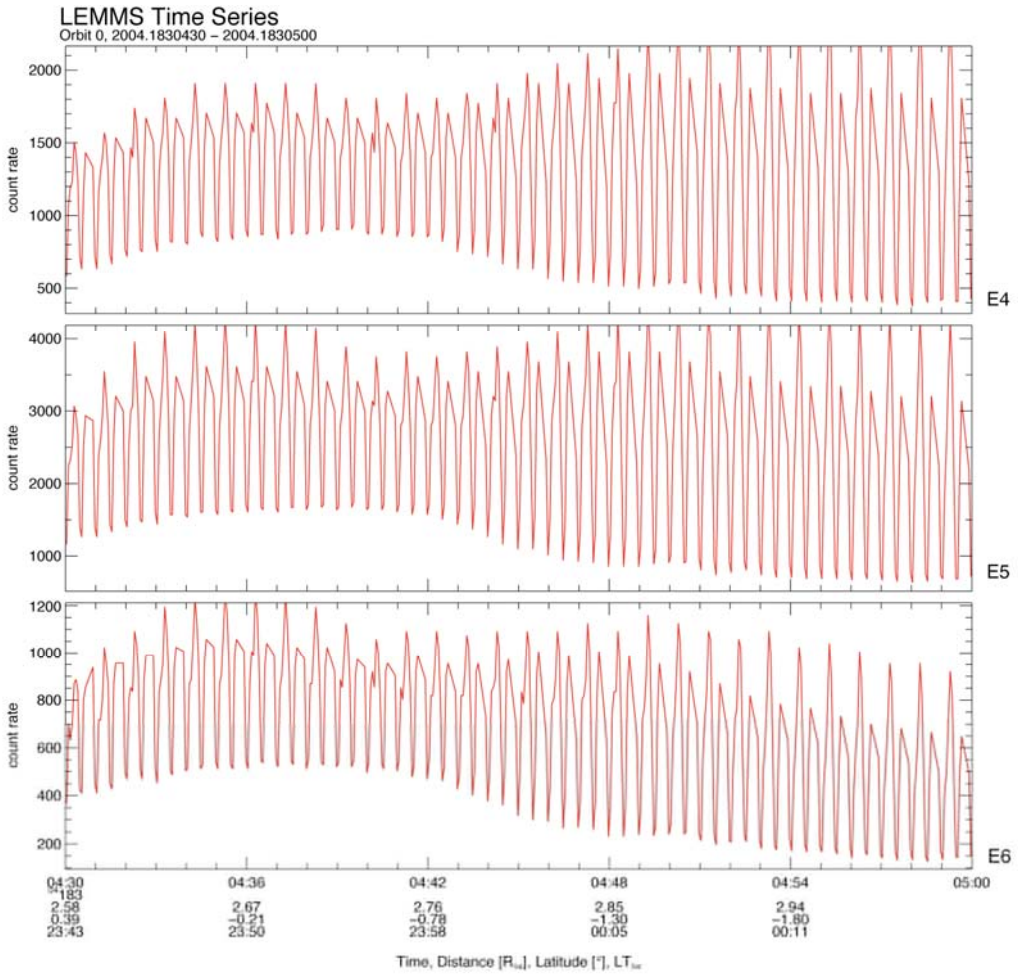

Figure S3: LEMMS data taken during the outbound G-ring crossing of 1 July 2004. Each panel shows the time series in one LEMMS channel. Sinusoidal variations in the fluxes occur because the instrument continuously scanned over a range of pitch angles.

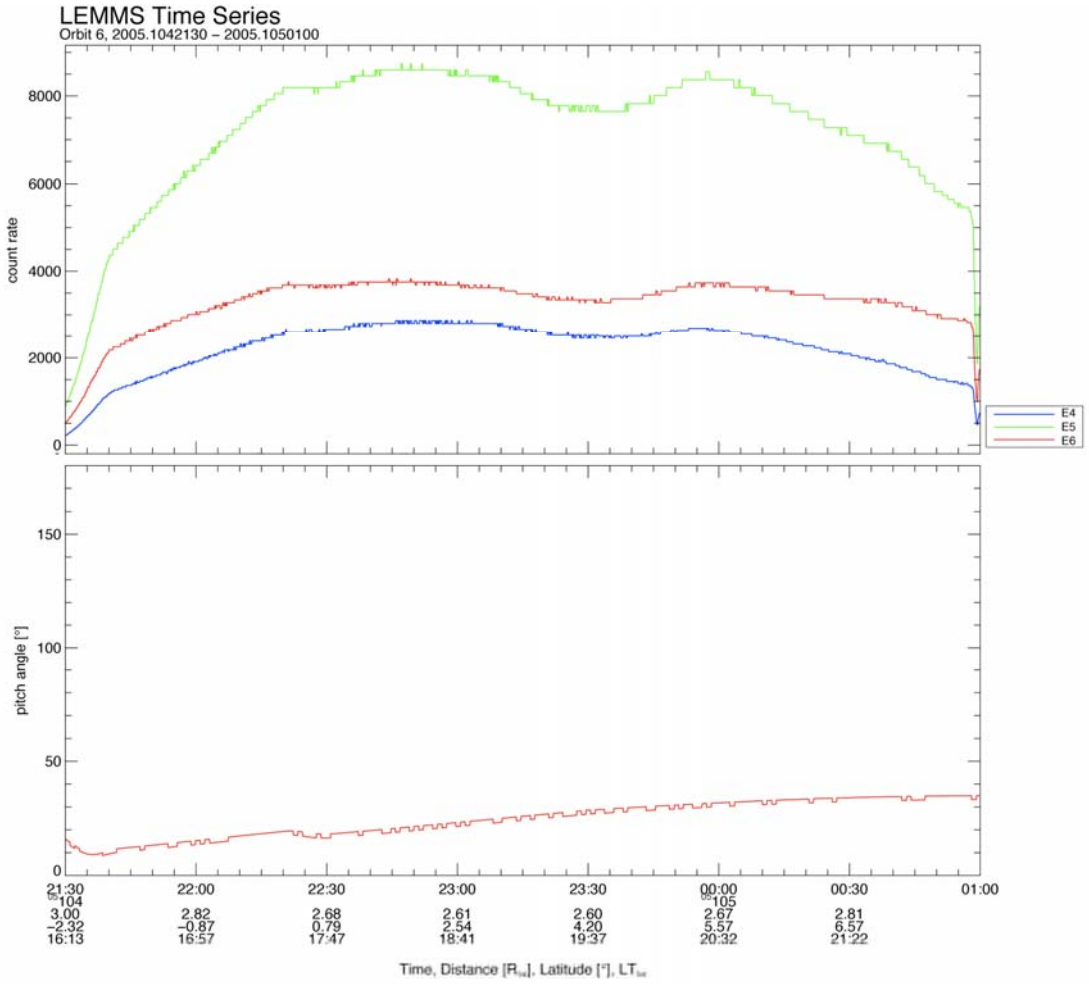

Figure S4: LEMMS data from the G-ring crossing of 14 Apr 2005. Top panel shows the time series of LEMMS channels E4-E6. The bottom panel shows the electron pitch angles observed by LEMMS during this time based on the orientation of the spacecraft. The bottom axis gives the day of year and time during the observation, as well as the spacecraft location in terms of L-shell, latitude and the local time. There is no indication of sharp electron absorptions in these data.

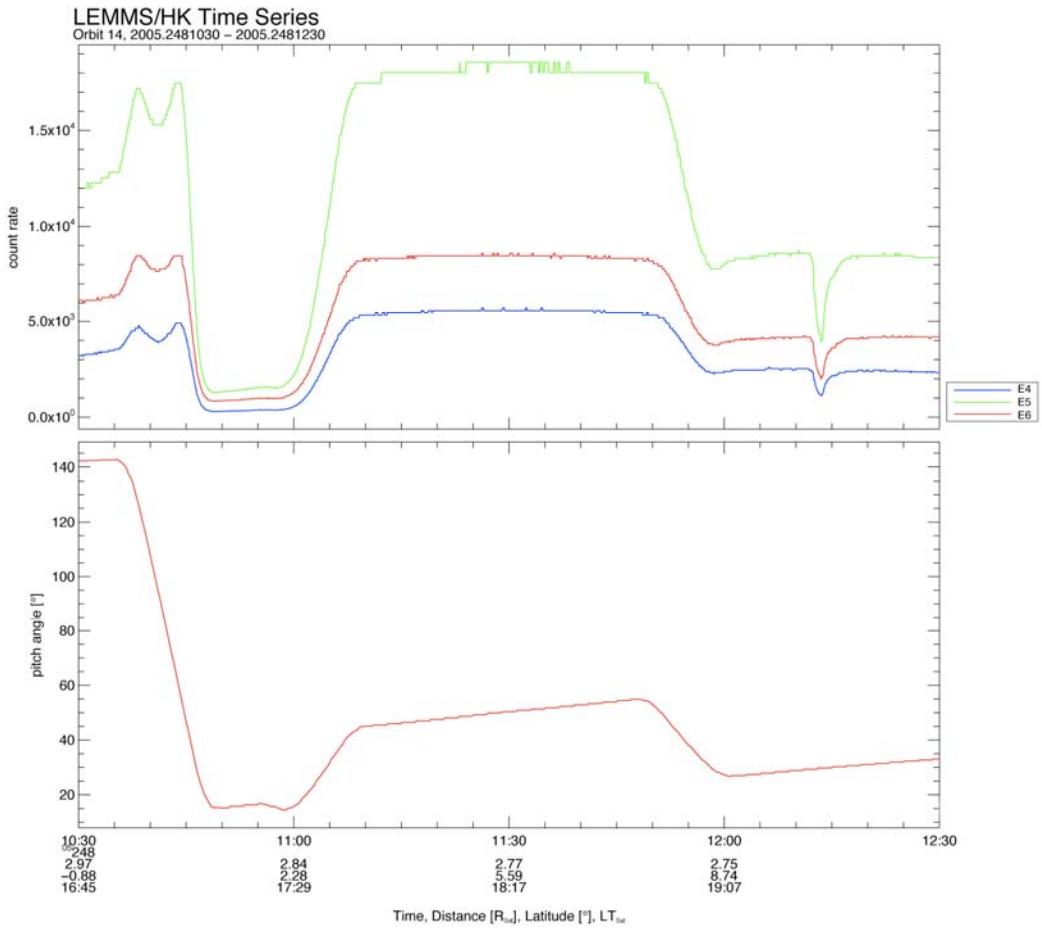

Figure S5: The time series of the LEMMS data in the E4-E6 channels during the periapsis of 5 Sep 2005, along with the electron pitch angles determined by the spacecraft orientation (see Fig. S3). During the plotted time interval, Cassini made a high latitude crossing of the magnetic field lines that thread the G-ring arc and observed electron depletion at ~12:13, during the outbound pass. The corresponding inbound signature, if present, was likely masked by one of the spacecraft re-orientation maneuvers during this period. These changes in LEMMS pointing are primarily responsible for the large changes in count rate and pitch angle coverage. The small flux variation observed between 11:55 and 12:00 may be the best candidate for being an inbound absorption signature by the arc.

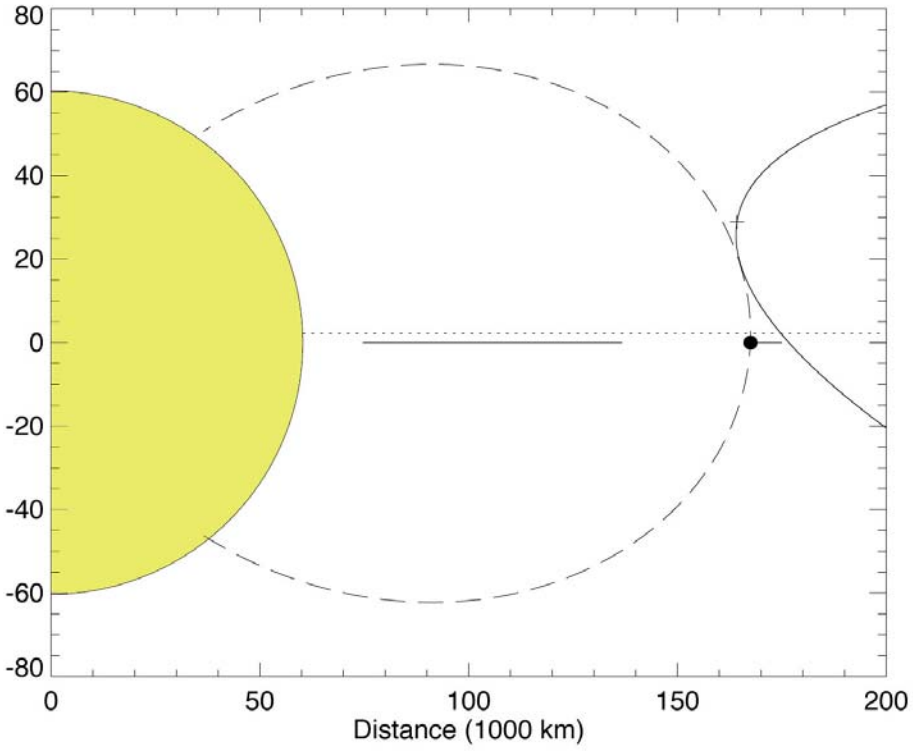

Figure S6: Vertical geometry of Cassini's 5 Sep 2005 passage near the G ring. The yellow sphere represents Saturn, while the horizontal black line represents the main rings (A-C). The position of the arc is marked with the dot. The dotted line indicates the location of the magnetic equator, and the dashed line shows the magnetic field line connected to the arc assuming an unperturbed dipole field. The solid arc shows the track of the Cassini spacecraft, with the position of the deep absorption indicated by the plus sign.

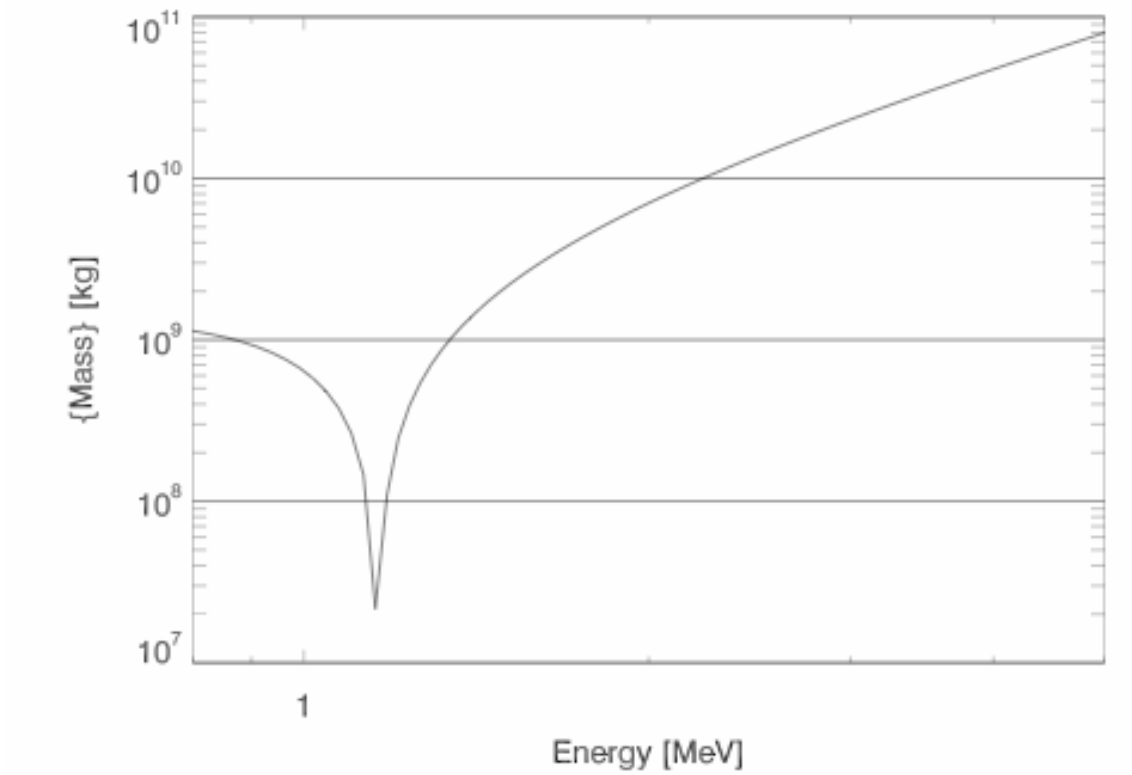

Figure S7: The total arc mass that is required to cause the observed electron absorption, as a function of electron energy.

Supporting Tables:

Table S1: ***ISS observations of G-ring****:*

Observation Date	File names	Ring Opening Angle[a] (degrees)	Phase Angle[b] (degrees)	Radial Resolution (km/pixel)	Range Integrated (km)
06 Sep 2004	N1472855263 N1473631252	16.9	84.0	55	167000-168000
24 May 2005	W1495621314 W1495623920 W1495626500 W1495629054 W1495631634 W1495634240 W1495636820 W1495639374	3.9	85.5	105	166000-169000
30 Oct 2005	N1509387606 through N1509395522 (72 images)	0.3	157.5	5	166000-169000
25 Apr 2006	N1524617785 through N1524648674 (18 images)	0.1	102.8	25	166000-169000
04 Jul 2006	N1530684463 N1530687000 N1530689537	0.7	144.9	25	165500-169500
19 Sep 2006	N1537362584 through N1537431998 (70 images)	10.0	162.5	15	166000-168500

[a]Angle between the ring plane and the light ray entering the camera from the ring.

[b]Angle between the incident ray from the sun and reflected ray from the ring.

Supporting References and Notes

S1. C. C. Porco *et al., Space Science Reviews* **115**, 363 (2004).
S2. M.R. Showalter, J.N. Cuzzi, *Icarus* **103** 124 (1993).
S3. R. A. Jacobson *et al.*, *Astron. J*. **132**, 2520 (2006).
S4. Available online http://www.boulder.swri.edu/hal/swift.html.
S5. Wisdom, M. Holman, *Astron. J*. **102**, 1528 (1991).
S6. M. J. Duncan, H. F. Levison, M. H. Lee, *Astron. J*. **116**, 2067 (1998).
S7. Available online ftp://naif.jpl.nasa.gov/pub/naif/generic_kernels/spk
S8. N. Borderies, P.-Y. Longaretti, *Icarus* **72,** 593 (1987).
S9. P.-Y. Longaretti, N. Borderies, *Icarus* **94**, 165 (1991).
S10. N. Borderies-Rappaport, P.-Y. Longaretti, *Icarus* **107**, 129 (1994).
S11. S. Renner, B. Sicardy, *Celest. Mech. Dyn. Astron*. **94**, 237 (2006).
S12. Y. Kozai, *Ann. Tokyo Astron. Obs*. **5**, 73 (1957).
S13.R. A. Jacobson, J. Spitale, C. C. Porco, W. M. Owen, *Astron. J*. **132**, 711 (2006).
S14. S. M. Krimigis *et al., Space Science Reviews* **114**, 233 (2004).
S15. Roussos, E. *et al., Icarus* accepted manuscript (2007).
S16. G. H. Jones *et al., Science* **311**, 1412 (2006).
S17. http://physics.nist.gov/PhysRefData/Star/Text/ESTAR.html
S18. J. N. Cuzzi, J. A. Burns *Icarus* **74** 284 (1988).
S19. M. F. Thomsen, J. A. Van Allen , *J. Geophys. Res.* **85** A115831 (1980)